

Symmetry-driven anisotropic coupling effect in antiferromagnetic topological insulator: Mechanism for high-Chern-number quantum anomalous Hall state

Yiliang Fan¹, Huaiqiang Wang^{2,*}, Peizhe Tang^{3,4}, Shuichi Murakami⁵, Xiangang Wan^{1,6}, Haijun Zhang^{1,6,*}, and Dingyu Xing^{1,6}
¹ National Laboratory of Solid State Microstructures and School of Physics, Nanjing University, Nanjing 210093, China
² School of Physics and Technology, Nanjing Normal University, Nanjing 210023, China
³ School of Materials Science and Engineering, Beihang University, Beijing 100191, China
⁴ Max Planck Institute for the Structure and Dynamics of Matter, Center for Free Electron Laser Science, Hamburg 22761, Germany
⁵ Department of Physics, Tokyo Institute of Technology, Tokyo 152-8551, Japan
⁶ Collaborative Innovation Center of Advanced Microstructures, Nanjing University, Nanjing 210093, China

Antiferromagnetic (AFM) topological insulators (TIs), which host magnetically gapped Dirac-cone surface states and exhibit many exotic physical phenomena, have attracted great attention. Here, we find that the coupled surface states can be intertwined to give birth to a set of $2n$ unique new Dirac cones, dubbed intertwined Dirac cones, through the anisotropic coupling enforced by crystalline n -fold ($n = 2, 3, 4, 6$) rotation symmetry C_{nz} in the presence of a PT -symmetry breaking potential, for example, an electric field. Interestingly, we also find that the warping effect further drives the intertwined Dirac-cone state into a quantum anomalous Hall phase with a high Chern number ($C = n$). Then, based on first-principles calculations, we have explicitly demonstrated six intertwined Dirac cones and a Chern insulating phase with a high Chern number ($C = 3$) in $\text{MnBi}_2\text{Te}_4/(\text{Bi}_2\text{Te}_3)_m/\text{MnBi}_2\text{Te}_4$ heterostructures, as well as the $C = 2$ and $C = 4$ phases in HgS and $\alpha\text{-Ag}_2\text{Te}$ films, respectively. This work discovers the intertwined Dirac-cone state in AFM TI thin films, which reveals a mechanism for designing the quantum anomalous Hall state with a high Chern number and also paves a way for studying highly tunable high-Chern-number flat bands of twistrionics.

I. INTRODUCTION

The interplay between magnetism and topology in condensed matters has greatly enriched the research content of topological quantum physics with many exotic physical phenomena, such as quantum anomalous Hall effect (QAHE) [1–5], magnetic Weyl semimetals [6, 7], topological magnetoelectric effects [8, 9], axion polariton [10–13] and so on. Recently, MnBi_2Te_4 and its family were discovered to be an important class of promising intrinsic magnetic topological insulators (TIs) and have attracted great attention [14–39]. Interestingly, the layer Hall effect was demonstrated in even-septuple-layer (SL) MnBi_2Te_4 films hosting two separated magnetically gapped Dirac cones exhibiting half-integer quantized Hall conductivity with opposite signs on the top and bottom surfaces [33]. The coupling between these two topological surface states play a crucial role in the low-energy physics especially for a thin TI film. Generally speaking, due to the n -fold ($n = 2, 3, 4, 6$) crystalline rotation symmetry (C_{nz}) that a (magnetic) TI usually respects, the surface-state

coupling should contain both isotropic terms [40–45] and symmetry-enforced anisotropic terms [46]. However, to our knowledge, the latter is significantly underrated in the literature and has not been fully appreciated before.

Remarkably, in this work, we find that the C_{nz} -symmetry-enforced anisotropic coupling can induce a set of $2n$ new Dirac cones, termed intertwined Dirac cones, around the Γ point through intertwining the two original Dirac cones on the top and bottom surfaces of an antiferromagnetic (AFM) TI thin film under a PT -symmetry breaking potential, e.g. an out-of-plane electric field. More intriguingly, when further considering the symmetry-enforced warping effect, an electrically tunable high-Chern-number ($|C| = n$) QAHE [47–50] can appear. These are further explicitly verified by the existence of six intertwined Dirac cones and corresponding $|C| = 3$ Chern insulating phase in $\text{MnBi}_2\text{Te}_4/(\text{Bi}_2\text{Te}_3)_m/\text{MnBi}_2\text{Te}_4$ ($m = 0, 1, 2$) heterostructures through first-principles calculations, and also confirmed in HgS [51] and $\alpha\text{-Ag}_2\text{Te}$ [52] films with C_{2z} and C_{4z} symmetries, respectively, via magnetic proximity effect on the surfaces. Our work not only reveals a concept of intertwined Dirac cones, but also provides a scheme to achieve high-Chern-number QAHE and paves a way to study highly tunable high-Chern-number flat

* zhanghj@nju.edu.cn; hqwang@nju.edu.cn

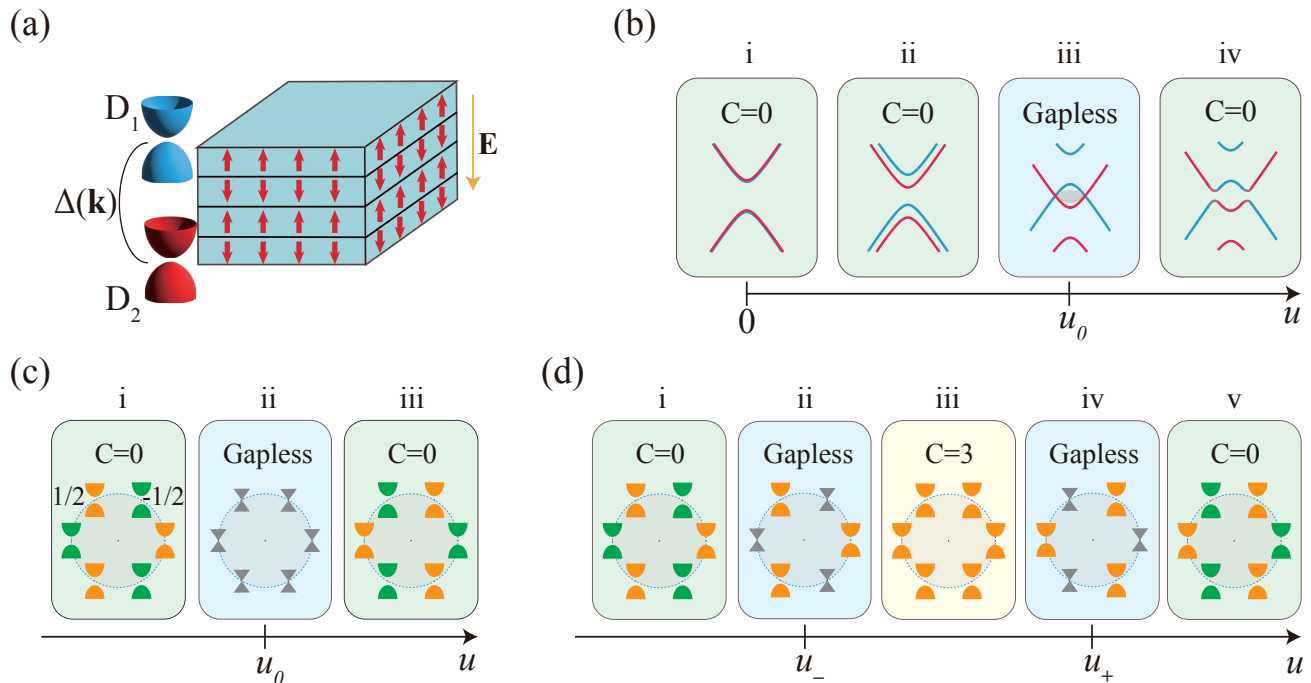


FIG. 1. (a) Schematic of the AFM TI thin film with coupled top and bottom Dirac-cone surface states. (b) The surface states are doubly degenerate when the PT symmetry is preserved (i). A PT -breaking potential u from the electric field can shift the surface Dirac cones to split the degenerate bands (ii). When only considering isotropic couplings, the energy gap first closes along a nodal ring at $u = u_0$ (iii) and reopens (iv), but without a topological transition. For an AFM TI film with C_{3z} symmetry, (c) the emergence of six intertwined Dirac cones from splitting the nodal ring by the anisotropic coupling. The color of Dirac cones indicates the different Chern number, with green (orange) representing $C = -1/2$ ($C = 1/2$). (d) The emergence of the high-Chern-number phase with $C = 3$ when further considering the symmetry-enforced warping effect, where the green (orange) intertwined Dirac cone changes its Chern number by 1 (-1) at the transition point of $u = u_-$ ($u = u_+$).

bands of twistrionics in AFM TI films.

II. METHODS

The first-principles calculations are carried out using the Perdew-Burke-Ernzerhof-type (PBE) generalized gradient approximation (GGA) [53] of the density functional theory (DFT), using the Vienna *ab initio* simulation package (VASP) [54]. The spin-orbit coupling is included in the DFT calculations. We take the GGA + U method with $U = 5.0$ eV to investigate the correlation effects. For the three materials: $\text{MnBi}_2\text{Te}_4/(\text{Bi}_2\text{Te}_3)_m/\text{MnBi}_2\text{Te}_4$ heterostructures, HgS and $\alpha\text{-Ag}_2\text{Te}$, we use a kinetic energy cutoff of 410 eV, 390 eV, and 380 eV, and a k-point mesh of $11 \times 11 \times 1$, $9 \times 9 \times 9$, and $10 \times 10 \times 8$, respectively. We use the experimental lattice constants of MnBi_4Te_7 ($a = 4.355$ Å and $c = 23.815$ Å) [55] to construct the $\text{MnBi}_2\text{Te}_4/(\text{Bi}_2\text{Te}_3)_m/\text{MnBi}_2\text{Te}_4$ heterostructures. These heterostructures are fully optimized until the force on each atom is less than 0.01 eV/Å. The optimized lattice constants are $a = 4.274$ Å ($m=0$), $a = 4.301$ Å ($m=1$) and $a = 4.311$ Å ($m=2$). Because they are two-dimensional heterostructures, we just list

the in-plane lattice constants here. The lattice constants of HgS ($a = 5.85$ Å) and $\alpha\text{-Ag}_2\text{Te}$ ($a = 6.8$ Å) are obtained from previous works [51, 52]. To simulate the uniaxial compressive strain applied to $\alpha\text{-Ag}_2\text{Te}$, we elongate the in-plane lattice parameter “ a ” and compress the out-of-plane parameter “ c ,” while keeping the cell volume unchanged. The same method has been employed in Ref. [56, 57]. As a result, we obtain $a = 6.89$ Å and $c = 6.67$ Å, resulting in a c/a ratio of 0.97.

Based on the results of the DFT calculations, we construct the maximally localized Wannier functions (MLWFs) [58, 59] using the WANNIER90 package [60]. During the construction of the MLWFs, we select the following orbitals: Mn-d, Bi-p, and Te-p for the $\text{MnBi}_2\text{Te}_4/(\text{Bi}_2\text{Te}_3)_m/\text{MnBi}_2\text{Te}_4$ heterostructures; Hg-s, Hg-d, and S-p for HgS; and Ag-s, Ag-d, and Te-p for $\alpha\text{-Ag}_2\text{Te}$.

We obtain the Wannier-based tight-binding Hamiltonian after constructing the MLWFs. We utilize the WannierTools package [61] to construct the N -cell-slab tight-binding Hamiltonians for HgS and $\alpha\text{-Ag}_2\text{Te}$, incorporating magnetic proximity effects and electric fields based on their respective bulk tight-binding Hamiltonians. To simulate the magnetic proximity effect, we add opposite Zeeman coupling energies of 0.05 eV and -0.05 eV to

the top and bottom cells, respectively, of the N -cell-slab tight-binding Hamiltonian. To simulate the electric field, we add an onsite potential to each orbital. The value of this potential equals the z coordinate of the Wannier center of the orbital multiplied by the value of the electric field. The calculations of the topological properties of the three materials are also conducted using the WannierTools package.

III. INTERTWINED DIRAC-CONE STATES

We start from an AFM TI thin film with two Dirac-cone surface states located on the top and bottom surfaces, respectively, as illustrated in Fig. 1(a). Due to the out-of-plane surface magnetic moments, each of them can be described by $H_{D_\alpha} = \hbar v(k_x \sigma_y - k_y \sigma_x) + m_\alpha \sigma_z$, where $\alpha = 1, 2$, D_1 (D_2) represents the top (bottom) Dirac cone, v is the Fermi velocity, $s = +(-)$ for the Dirac cone D_1 (D_2), the Planck's constant \hbar is simply set as 1 henceforth, and m_α indicates Zeeman coupling. Since magnetic moments are opposite on the two surfaces, we have $m_1 = -m_2 = m$ (m is set to be positive henceforth). In the basis of $|D_1, \uparrow\rangle, |D_1, \downarrow\rangle, |D_2, \uparrow\rangle, |D_2, \downarrow\rangle$, where \uparrow (\downarrow) represents the spin, a four-band low-energy Hamiltonian of the two uncoupled Dirac cones is directly written as

$$H_0 = v\tau_z \otimes (k_x \sigma_y - k_y \sigma_x) + m\tau_z \otimes \sigma_z. \quad (1)$$

Here, the Pauli matrix τ_z acts in the subspace of top and bottom Dirac cones. This Hamiltonian describes two degenerate Dirac cones with a gap of $2m$, as shown in Fig. 1(b)(i). Although the time-reversal ($T = i\sigma_y K$ with K denoting the complex conjugate) and inversion ($P = \tau_x$) symmetries are separately broken, the combined PT symmetry is preserved, which ensures the double degeneracy of each band. We then introduce a PT -symmetry breaking potential u between the two Dirac cones described by $H_u = u\tau_z \otimes \sigma_0$, which could be induced by an out-of-plane electric field ($u \propto E$). This potential lifts the double degeneracy of each band by conversely shifting the two spatially separated Dirac cones in energy [see Fig. 1(b)(ii)]. With increasing u , the energy gap gradually reduces until it closes at Γ when $u = m$. Further increase of u , i.e., $u > m$, will expand the closing point into a nodal ring.

Now we consider the coupling between D_1 and D_2 . When assuming that the AFM TI respects C_{nz} ($n = 2, 3, 4, 6$) rotation symmetry and a combined symmetry $M_x T$ of mirror and time-reversal operations, we can obtain the following coupling Hamiltonian [see the Supplemental Material (SM) [62] for more details]:

$$H_{\text{coup}} = (\Delta - Bk^2)\tau_x \otimes \sigma_0 + R_1 g_n(k_x, k_y)\tau_y \otimes \sigma_0, \quad (2)$$

where $k^2 = k_x^2 + k_y^2$ and $g_n(k_x, k_y) = (k_+^n - k_-^n)/2i$ with $k_\pm = k_x \pm ik_y$, and i is the imaginary unit. The first term in Eq. (2) describes isotropic couplings up to k^2 order ($\Delta B > 0$ is assumed throughout the work [41]),

while the second term comes from the symmetry-enforced anisotropic coupling (for simplicity we have dropped other higher-order coupling terms which will not affect our main results [62]). Most importantly, it plays a crucial role in generating intertwined Dirac-cone states, as shown below. Without the anisotropic coupling, the energy gap closes along a nodal ring with the radius $k_0 = \sqrt{\Delta/B}$ at $u = u_0 = \sqrt{m^2 + v^2 \Delta/B}$ [see Fig. 1(b)(iii)], and it reopens when $u > u_0$ [see Fig. 1(b)(iv)]. However, there is no topological phase transition in this gap-closing-and-reopening process, for the Chern number remains zero. Interestingly, due to the anisotropic coupling, the nodal ring at $u = u_0$ splits into $2n$ nodal points connected to each other by C_{nz} symmetry, as illustrated in Fig. 1(c)(ii). In the k - θ polar coordinate, these nodal points are located at (k_0, θ_j) , where $\theta_j = j\pi/n$, with $j = 0, 1, 2, \dots, 2n-1$. Only at these nodal points does the coupling become zero, and by expanding the Hamiltonian around them to linear order, we obtain a low-energy Dirac Hamiltonian as

$$h_n(\theta_j) = -2Bk_0 q_\rho \sigma_x + (-1)^j n R_1 k_0^{n-1} q_\theta \sigma_y + \delta u \sigma_z, \quad (3)$$

where $q_\rho = k - k_0$ and $q_\theta = k_0 \delta\theta$ with $\delta\theta = \theta - \theta_j$, are the momenta measured from each nodal point along the radial and angular directions in the polar coordinates and $\delta u = u - u_0$. The effective Hamiltonian $h_n(\theta_j)$ indicates that each nodal point is a new Dirac-cone state with a mass of δu . Since this set of Dirac-cone states emerge from the coupling between the top and bottom surface states, they are dubbed "intertwined" Dirac-cone states. Moreover, according to Eq. (3), the helicity of the intertwined Dirac-cone state labeled by odd or even value of j is opposite. Consequently, its Chern number, given by $C(\theta_j) = \frac{(-1)^{j+1}}{2} \text{sgn}(\delta u)$, becomes opposite for odd and even j [see Fig. 1(c)(i)]. When δu changes from negative ($u < u_0$) to positive ($u > u_0$), $C(\theta_j)$ changes by $+1$ (-1) for odd (even) j [see Fig. 1(c)(iii)], so the total Chern number still equals zero. To exemplify this, we have chosen $n = 3$ to numerically calculate typical Berry curvature distributions of the valence bands near the transition point with $u < u_0$ [Fig. 2(e)(i)] and $u > u_0$ [Fig. 2(e)(ii)], as well as the band structure of the massless intertwined Dirac-cone states at the transition point of $u = u_0$ [Fig. 2(a)]. Obviously, the local Berry curvature around each intertwined Dirac-cone state changes its sign between $u < u_0$ and $u > u_0$, and it is always opposite between odd and even j , leading to a zero net Chern number.

Furthermore, we have also investigated how the layer Hall effect is affected by the coupling between surface states. In Fig. 2(c), we have plotted the layer-resolved Hall conductivity (LRHC) versus the potential u . With increasing u , the LRHCs of both surfaces gradually decrease toward zero. Note that the deviation from the quantized value $\pm e^2/2h$ before the gap closing ($u < u_0$) results from the coupling between the surface states.

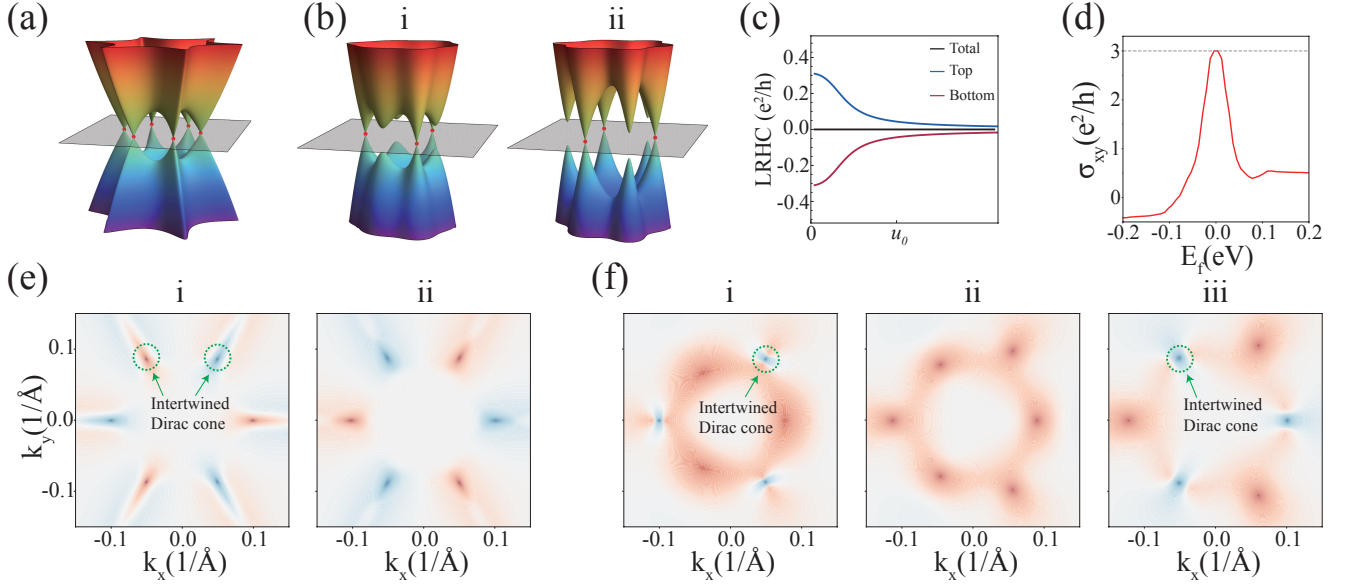


FIG. 2. The band structures for (a) the six massless intertwined Dirac cones at the critical potential $u = u_0$ without the warping effect, and (b) the two sets of three massless intertwined Dirac cones at the gap-closing point of $u = u_-$ (i) and $u = u_+$ (ii). (c) The layer-resolved Hall conductivity (LRHC) for the top (blue line) and bottom (red line) surfaces. (d) The anomalous Hall conductivity (AHC) for the $u_- < u < u_+$ case, where the AHC equals $3 e^2/h$ when the Fermi level lies in the energy gap. (e) Without the warping effect, the Berry curvatures for $u < u_0$ (i) and $u > u_0$ (ii), respectively. (f) With the warping effect, typical Berry curvatures for $u < u_-$ ($C = 0$) (i), $u_- < u < u_+$ ($C = 3$) (ii), and $u > u_+$ ($C = 0$) (iii), respectively. The parameters are chosen as $m = 0.05$ eV, $v = 1$ eV $\cdot \text{\AA}$, $\Delta = 0.05$ eV, $B = 5$ eV $\cdot \text{\AA}^2$, $R_1 = 100$ eV $\cdot \text{\AA}^3$, and $R_2 = 100$ eV $\cdot \text{\AA}^3$ in the numerical calculations.

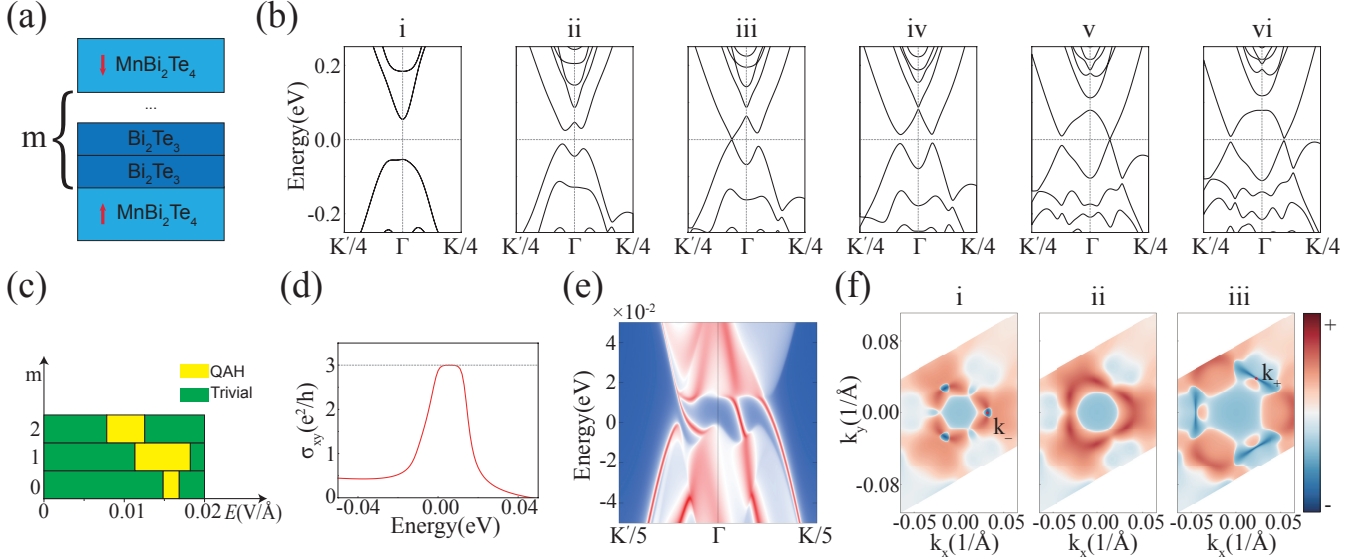


FIG. 3. (a) Schematic of the $\text{MnBi}_2\text{Te}_4 / (\text{Bi}_2\text{Te}_3)_m / \text{MnBi}_2\text{Te}_4$ ($m = 0, 1, 2$) heterostructure structure. (b) The band structures for $m = 1$ with increasing the electric field, where $E = 0.0$ V/ \AA (i), 0.008 V/ \AA (ii), 0.0113 V/ \AA (iii), 0.0135 V/ \AA (iv), 0.0182 V/ \AA (v), and 0.02 V/ \AA (vi). (c) The topological phase diagram for different values of m , where the yellow (green) region denotes the topologically nontrivial (trivial) phase with $C = 3$ ($C = 0$). (d), (e) The AHC and chiral edge states for the $C = 3$ phase at $E = 0.0135$ V/ \AA for $m = 1$. A quantized value of $\sigma_{xy} = 3 e^2/h$ can be seen in (d) when the Fermi level is in the energy gap, which originates from the emergence of three chiral edge states shown in (e). (f) Berry curvatures for $E = 0.011$ V/ \AA ($u < u_-$ with $C = 0$) (i), $E = 0.0135$ V/ \AA ($u_- < u < u_+$ with $C = 3$) (ii), and $E = 0.0186$ V/ \AA ($u > u_+$ with $C = 0$) (iii). Significant changes of Berry curvatures are seen around the intertwined Dirac cones located at k_- (k_+) in the first (second) topological phase transition.

IV. WARPING EFFECT AND HIGH-CHERN-NUMBER PHASE

Based on the above analysis, we now reveal the emergence of a high-Chern-number phase with $|C| = n$ by further considering the symmetry-enforced warping effect [63, 64] of the two original Dirac-cone surface states. The warping effect can be described by the Hamiltonian $H_{\text{warp}} = R_2 w_n(k_x, k_y) \tau_z \otimes \sigma_z$, where $w_n(k_x, k_y) = (k_x^n + k_y^n)/2$. Because of H_{warp} , the critical potential u_0 of the gap-closing condition for each intertwined Dirac-cone state now becomes [62]

$$u_{0,j} = \sqrt{\left[m + (-1)^j R_2 (\Delta/B)^{n/2} \right]^2 + v^2 \Delta/B}. \quad (4)$$

In contrast to the case without the warping effect where $u_{0,j}$ is identical for all values of j , the critical gapless transition point is now distinct between odd and even j , namely, $u_{0,j} \equiv u_-$ (u_+) for odd (even) j . This can be understood from the fact that H_{warp} effectively introduces opposite corrections to the Zeeman term between intertwined Dirac cones with odd and even j . The difference between u_{\pm} indicates that the changes of Chern number ΔC of intertwined Dirac-cone states with odd j ($\Delta C = +1$) and even j ($\Delta C = -1$) no longer occur simultaneously [see Figs. 1(d)(ii) and 1(d)(iv)]. Therefore, if $mR_2 > 0$ is assumed, we have $u_- < u_+$ and a high-Chern-number phase with $C = n$ when $u_- < u < u_+$, while $C = 0$ for both $u > u_+$ and $u < u_-$, as exemplified by the $C = 3$ case in Fig. 1(d). We have also calculated the Berry curvature distribution of the valence bands with $u < u_-$ [Fig. 2(f)(i)], $u_- < u < u_+$ [Fig. 2(f)(ii)], and $u > u_+$ [Fig. 2(f)(iii)]. The band structures at the critical transition points of $u = u_-$ and $u = u_+$ are presented in Figs. 2(b)(i) and 2(b)(ii), respectively. The sign change of the Berry curvature around each intertwined Dirac-cone state across the transition points of u_{\pm} can be clearly seen in Fig. 2(f). Moreover, to verify the high-Chern-number phase for $u_- < u < u_+$, we have calculated the anomalous Hall conductivity (AHC) in Fig. 2(d), where the AHC exactly equals $3 e^2/h$ when the Fermi energy lies in the gap.

V. MATERIAL REALIZATION

A. $\text{MnBi}_2\text{Te}_4 / (\text{Bi}_2\text{Te}_3)_m / \text{MnBi}_2\text{Te}_4$

Inspired by recent experimental progress on MnBi_2Te_4 family intrinsic AFM TIs and related heterostructures, such as MnBi_4Te_7 and $\text{MnBi}_6\text{Te}_{10}$ [25, 55, 65–72], we take the $\text{MnBi}_2\text{Te}_4 / (\text{Bi}_2\text{Te}_3)_m / \text{MnBi}_2\text{Te}_4$ ($m = 0, 1, 2$) heterostructure as a realistic example of the preceding $n = 3$ case with the C_{3z} symmetry and perform first-principles calculations to demonstrate the existence of six intertwined Dirac-cone states and a high-Chern-number ($C = 3$) QAHE. As shown in Fig. 3(a), the

$\text{MnBi}_2\text{Te}_4 / (\text{Bi}_2\text{Te}_3)_m / \text{MnBi}_2\text{Te}_4$ heterostructure is constructed by inserting m Bi_2Te_3 quintuple-layers between two MnBi_2Te_4 SLs, which preserves the required C_{3z} and the combined $M_x T$ symmetries. Moreover, according to the total energy calculation [62], the out-of-plane AFM order is found to be the magnetic ground state.

First, we inspect the band structure of the $\text{MnBi}_2\text{Te}_4 / \text{Bi}_2\text{Te}_3 / \text{MnBi}_2\text{Te}_4$ heterostructure with increasing the out-of-plane electric field. Without the electric field, the band structure is doubly degenerate with an energy gap [see Fig. 3(b)(i)]. Once a weak electric field is applied (e.g. $E = 0.008 \text{ V/\AA}$), the band structure starts splitting due to breaking the PT symmetry, seen in Fig. 3(b)(ii). With increasing the electric field, the band structure undergoes two successive gap-closing-and-reopening processes [see Figs. 3(b)(iii) and (v)], where the gap closes at $E = 0.0113 \text{ V/\AA}$ and $E = 0.0182 \text{ V/\AA}$, respectively. Next, we investigate topological properties, namely, Berry curvatures and corresponding Chern numbers for different regions of the electric field. The Chern number is calculated to be $C = 3$ in the intermediate region between the two gap-closing processes, whereas $C = 0$ for the other two regions (see the Wilson-loop [73] calculations in the SM [62]), which is well consistent with the above model prediction. Moreover, we have calculated the AHC in the $C = 3$ region [see Fig. 3(d)], which takes the expected value of $\sigma_{xy} = 3 e^2/h$ when the Fermi level lies in the gap. This is further confirmed by the emergence of three chiral edge states in the energy gap [see Fig. 3(e)]. Typical Berry curvatures for the three regions are shown in Fig. 3(f), where significant changes of the Berry curvature occur around the points of intertwined Dirac cones, reflecting their pivotal role in realizing the high-Chern-number QAHE. Similar topological phase diagrams can be found for other values of m , as shown in Fig. 3(c) [62].

B. HgS and $\alpha\text{-Ag}_2\text{Te}$

We choose HgS and $\alpha\text{-Ag}_2\text{Te}$ as realistic materials to realize the models for $n = 2$ and $n = 4$, respectively. HgS is a topological insulator respecting C_{2z} symmetry [51]. $\alpha\text{-Ag}_2\text{Te}$ is a zero-gap semiconductor respecting C_{4z} symmetry with inverted band structure [52]. Thus, we apply a uniaxial compressive strain along the "c" axis, resulting in $c/a = 0.97$ ($c/a = 1$ before applying strain), to open a small gap at the Γ point. Moreover, since HgS and $\alpha\text{-Ag}_2\text{Te}$ are nonmagnetic, for each material, we have constructed a N -cell-slab tight-binding model along the out-of-plane direction based on the first-principles calculations of the bulk electronic structures and suppose there are two ferromagnetic materials with opposite magnetic moments near the top and bottom surfaces of the slab separately. To simulate the magnetic proximity effect induced by the two ferromagnetic materials, we add opposite Zeeman coupling energies to the top (0.05 eV) and bottom (−0.05 eV) cells, respectively. Finally, the effect

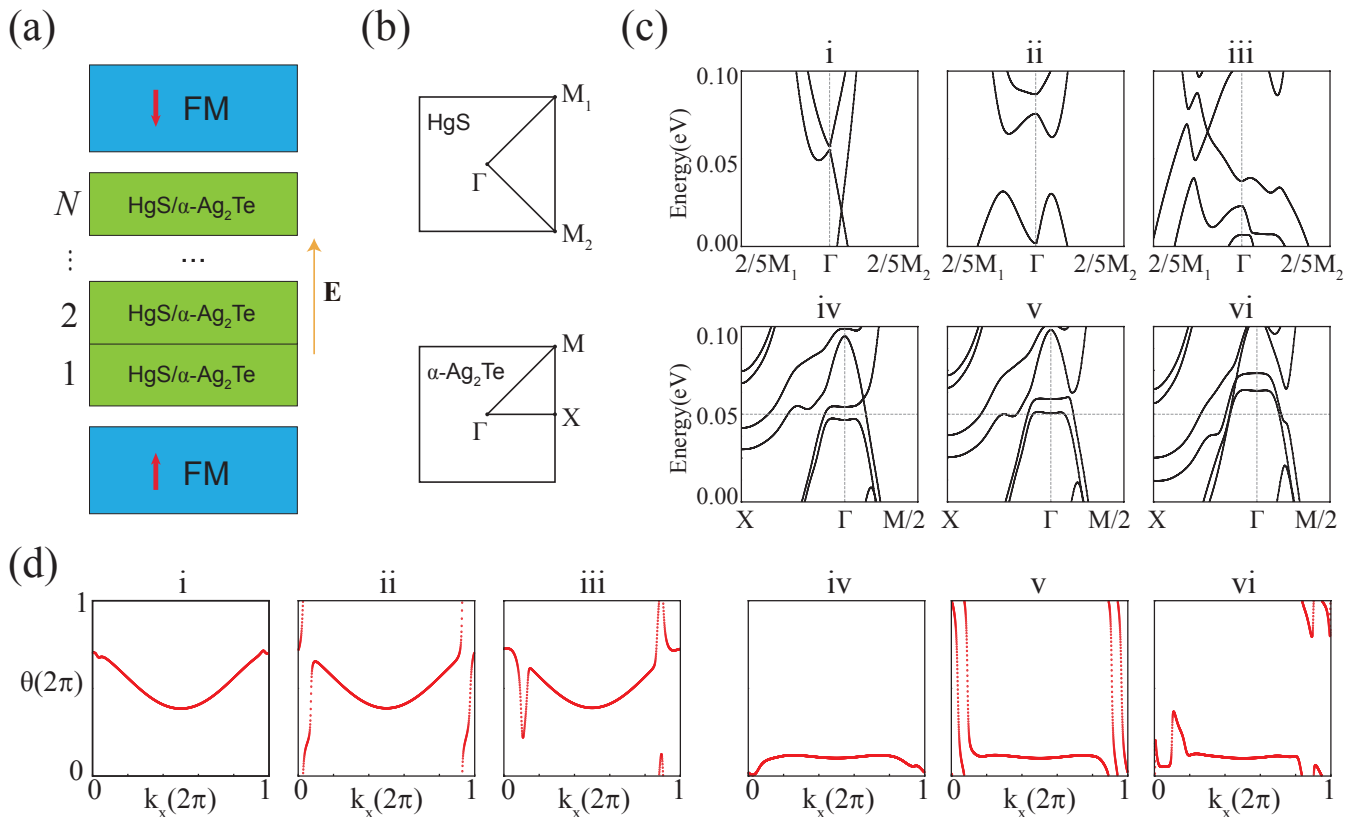


FIG. 4. (a) Schematic of the N -cell slab of HgS or α -Ag₂Te. The top and bottom surfaces of the slab are in proximity to ferromagnets with opposite magnetic moments. (b) The 2D Brillouin zone and high-symmetry points of HgS and α -Ag₂Te. (c) Band structures for HgS and α -Ag₂Te with increasing the electric field, where $E = 0.0233$ V/Å (i), 0.03 V/Å (ii), and 0.0384 V/Å (iii) for HgS and 0.027 V/Å (iv), 0.03 V/Å (v), and 0.039 V/Å (vi) for α -Ag₂Te. (d) Wilson-loops of HgS and α -Ag₂Te with increasing the electric field, where $E = 0.02$ V/Å (i), 0.03 V/Å (ii), and 0.04 V/Å (iii) for HgS and 0.014 V/Å (iv), 0.031 V/Å (v), and 0.041 V/Å (vi) for α -Ag₂Te.

of the out-of-plane electric field is simulated by adding an onsite potential to each orbital. The value of the potential equals the coordinates of the Wannier center of the orbital along the stacking direction multiplied by the value of the electric field.

For HgS and α -Ag₂Te, we have built a five-cell-slab and four-cell-slab tight-binding model, respectively, as shown in Fig. 4(a). Figure 4(c) shows the band structures of the model under different electric fields, where the high-symmetry points have been labeled in Fig. 4(b). We find that the energy gap for HgS closes at $E = 0.0233$ V/Å [Fig. 4(c)(i)] and 0.0384 V/Å [Fig. 4(c)(iii)], while for α -Ag₂Te, it closes at $E = 0.027$ V/Å [Fig. 4(c)(iv)] and 0.039 V/Å [Fig. 4(c)(vi)], respectively. Between the two electric field values, there is a $|C| = 2$ phase for HgS and $|C| = 4$ phase for α -Ag₂Te, which is verified by the calculations of the Wilson-loops in Fig. 4(d)(i)-(iii) (HgS) and Fig. 4(d)(iv)-(vi) (α -Ag₂Te). Figure 4(d)(ii) and Fig. 4(d)(v) clearly shows the existence of the $|C| = 2$ and $|C| = 4$ phase.

VI. CONCLUSION

In summary, we have considered the previously overlooked anisotropic coupling between Dirac-cone surface states of AFM TI thin films with n -fold rotational symmetry. Intriguingly, this coupling could lead to the emergence of $2n$ intertwined Dirac cones under an out-of-plane electric field, and a high-Chern-number phase with $|C| = n$ is predicted by tuning the electric field, which has been explicitly verified by first-principles calculations. The proposed intertwined Dirac-cone states are essentially different from conventional topological Dirac-cone surface states. The most unique advantage of the intertwined Dirac cones is the flexible electrical tunability, which could give rise to interesting physical phenomena. For example, a relative twist between the top and bottom surfaces of the AFM TI could result in flat bands with significantly reduced velocity of the intertwined Dirac-cone state, which may lead to high-Chern-number flat bands. More interestingly, the flat bands are expected to be greatly tuned by an electric field, which provides a new versatile platform for studying the interplay between

topology, magnetism, twistrionics, and strong correlation effects.

ACKNOWLEDGMENTS

This work is partly supported by National Key Projects for Research and Development of China (Grants No. 2021YFA1400400 and No. 2022YFA1403602), the

Fundamental Research Funds for the Central Universities (Grant No. 020414380185), the Natural Science Foundation of Jiangsu Province (No. BK20200007), the Natural Science Foundation of China (No. 12074181, No. 12104217, No. 12174182, No. 12234011, No. 12374053, and No. 11834006), and the e-Science Center of Collaborative Innovation Center of Advanced Microstructures. S. M. is supported by JSPS KAKENHI Grants No. JP22H00108 and No. JP22K18687 and MEXT Initiative to Establish Next-generation Novel Integrated Circuits Centers (X-NICS) Grant No. JPJ011438.

-
- [1] F. D. M. Haldane, Model for a quantum Hall effect without Landau levels: Condensed-matter realization of the "parity anomaly", *Phys. Rev. Lett.* **61**, 2015 (1988).
- [2] R. Yu, W. Zhang, H.-J. Zhang, S.-C. Zhang, X. Dai, and Z. Fang, Quantized anomalous Hall effect in magnetic topological insulators, *Science* **329**, 61 (2010).
- [3] C.-Z. Chang, J. Zhang, X. Feng, J. Shen, Z. Zhang, M. Guo, K. Li, Y. Ou, P. Wei, L.-L. Wang, Z.-Q. Ji, Y. Feng, S. Ji, X. Chen, J. Jia, X. Dai, Z. Fang, S.-C. Zhang, K. He, Y. Wang, L. Lu, X.-C. Ma, and Q.-K. Xue, Experimental observation of the quantum anomalous Hall effect in a magnetic topological insulator, *Science* **340**, 167 (2013).
- [4] Y. Deng, Y. Yu, M. Z. Shi, Z. Guo, Z. Xu, J. Wang, X. H. Chen, and Y. Zhang, Quantum anomalous Hall effect in intrinsic magnetic topological insulator MnBi_2Te_4 , *Science* **367**, 895 (2020).
- [5] C.-Z. Chang, C.-X. Liu, and A. H. MacDonald, Colloquium: Quantum anomalous Hall effect, *Rev. Mod. Phys.* **95**, 011002 (2023).
- [6] X. Wan, A. M. Turner, A. Vishwanath, and S. Y. Savrasov, Topological semimetal and fermi-arc surface states in the electronic structure of pyrochlore iridates, *Phys. Rev. B* **83**, 205101 (2011).
- [7] G. Xu, H. Weng, Z. Wang, X. Dai, and Z. Fang, Chern semimetal and the quantized anomalous Hall effect in HgCr_2Se_4 , *Phys. Rev. Lett.* **107**, 186806 (2011).
- [8] X.-L. Qi, T. L. Hughes, and S.-C. Zhang, Topological field theory of time-reversal invariant insulators, *Phys. Rev. B* **78**, 195424 (2008).
- [9] L. Wu, M. Salehi, N. Koirala, J. Moon, S. Oh, and N. Armitage, Quantized Faraday and Kerr rotation and axion electrodynamics of a 3D topological insulator, *Science* **354**, 1124 (2016).
- [10] R. Li, J. Wang, X.-L. Qi, and S.-C. Zhang, Dynamical axion field in topological magnetic insulators, *Nat. Phys.* **6**, 284 (2010).
- [11] D. M. Neno, C. A. Garcia, J. Gooth, C. Felser, and P. Narang, Axion physics in condensed-matter systems, *Nat. Rev. Phys.* **2**, 682 (2020).
- [12] Y. Xiao, H. Wang, D. Wang, R. Lu, X. Yan, H. Guo, C.-M. Hu, K. Xia, H. Zhang, and D. Xing, Nonlinear level attraction of cavity axion polariton in antiferromagnetic topological insulator, *Phys. Rev. B* **104**, 115147 (2021).
- [13] T. Zhu, H. Wang, D. Xing, and H. Zhang, Axionic surface wave in dynamical axion insulators, *Phys. Rev. B* **106**, 075103 (2022).
- [14] Y. Gong, J. Guo, J. Li, K. Zhu, M. Liao, X. Liu, Q. Zhang, L. Gu, L. Tang, X. Feng, D. Zhang, W. Li, C. Song, L. Wang, P. Yu, X. Chen, Y. Wang, H. Yao, W. Duan, Y. Xu, S.-C. Zhang, X. Ma, Q.-K. Xue, and K. He, Experimental realization of an intrinsic magnetic topological insulator, *Chin. Phys. Lett.* **36**, 076801 (2019).
- [15] M. M. Otrokov, I. I. Klimovskikh, H. Bentmann, D. Estyunin, A. Zeugner, Z. S. Aliev, S. Gass, A. U. B. Wolter, A. V. Koroleva, A. M. Shikin, M. Blanco-Rey, M. Hoffmann, I. P. Rusinov, A. Y. Vyazovskaya, S. V. Ereemeev, Y. M. Koroteev, V. M. Kuznetsov, F. Freyre, J. Sanchez-Barriga, I. R. Amiraslanov, M. B. Babanly, N. T. Mamedov, N. A. Abdullayev, V. N. Zverev, A. Alfonso, V. Kataev, B. Buechner, E. F. Schwier, S. Kumar, A. Kimura, L. Petaccia, G. Di Santo, R. C. Vidal, S. Schatz, K. Kissner, M. Uenzelmann, C. H. Min, S. Moser, T. R. F. Peixoto, F. Reinert, A. Ernst, P. M. Echenique, A. Isaeva, and E. V. Chulkov, Prediction and observation of an antiferromagnetic topological insulator, *Nature* **576**, 416 (2019).
- [16] D. Zhang, M. Shi, T. Zhu, D. Xing, H. Zhang, and J. Wang, Topological axion states in the magnetic insulator MnBi_2Te_4 with the quantized magnetoelectric effect, *Phys. Rev. Lett.* **122**, 206401 (2019).
- [17] J. Li, Y. Li, S. Du, Z. Wang, B.-L. Gu, S.-C. Zhang, K. He, W. Duan, and Y. Xu, Intrinsic magnetic topological insulators in van der Waals layered MnBi_2Te_4 -family materials, *Sci. Adv.* **5**, eaaw5685 (2019).
- [18] B. Chen, F. Fei, D. Zhang, B. Zhang, W. Liu, S. Zhang, P. Wang, B. Wei, Y. Zhang, Z. Zuo, *et al.*, Intrinsic magnetic topological insulator phases in the Sb doped MnBi_2Te_4 bulks and thin flakes, *Nat. Commun.* **10**, 4469 (2019).
- [19] Y. J. Chen, L. X. Xu, J. H. Li, Y. W. Li, H. Y. Wang, C. F. Zhang, H. Li, Y. Wu, A. J. Liang, C. Chen, S. W. Jung, C. Cacho, Y. H. Mao, S. Liu, M. X. Wang, Y. F. Guo, Y. Xu, Z. K. Liu, L. X. Yang, and Y. L. Chen, Topological electronic structure and its temperature evolution in antiferromagnetic topological insulator MnBi_2Te_4 , *Phys. Rev. X* **9**, 041040 (2019).
- [20] H. Li, S.-Y. Gao, S.-F. Duan, Y.-F. Xu, K.-J. Zhu, S.-J. Tian, J.-C. Gao, W.-H. Fan, Z.-C. Rao, J.-R. Huang, J.-J. Li, D.-Y. Yan, Z.-T. Liu, W.-L. Liu, Y.-B. Huang, Y.-L. Li, Y. Liu, G.-B. Zhang, P. Zhang, T. Kondo, S. Shin, H.-C. Lei, Y.-G. Shi, W.-T. Zhang, H.-M. Weng, T. Qian, and H. Ding, Dirac surface states in intrinsic magnetic topological insulators EuSn_2As_2 and

- MnBi_{2n}Te_{3n+1}, *Phys. Rev. X* **9**, 041039 (2019).
- [21] Y.-J. Hao, P. Liu, Y. Feng, X.-M. Ma, E. F. Schwier, M. Arita, S. Kumar, C. Hu, R. Lu, M. Zeng, Y. Wang, Z. Hao, H.-Y. Sun, K. Zhang, J. Mei, N. Ni, L. Wu, K. Shimada, C. Chen, Q. Liu, and C. Liu, Gapless surface Dirac cone in antiferromagnetic topological insulator MnBi₂Te₄, *Phys. Rev. X* **9**, 041038 (2019).
- [22] M. M. Otrokov, I. P. Rusinov, M. Blanco-Rey, M. Hoffmann, A. Y. Vyazovskaya, S. V. Eremeev, A. Ernst, P. M. Echenique, A. Arnau, and E. V. Chulkov, Unique thickness-dependent properties of the van der Waals interlayer antiferromagnet MnBi₂Te₄ films, *Phys. Rev. Lett.* **122**, 107202 (2019).
- [23] H. Sun, B. Xia, Z. Chen, Y. Zhang, P. Liu, Q. Yao, H. Tang, Y. Zhao, H. Xu, and Q. Liu, Rational design principles of the quantum anomalous Hall effect in superlattice-like magnetic topological insulators, *Phys. Rev. Lett.* **123**, 096401 (2019).
- [24] J. Ge, Y. Liu, J. Li, H. Li, T. Luo, Y. Wu, Y. Xu, and J. Wang, High-Chern-number and high-temperature quantum Hall effect without Landau levels, *Nat. Sci. Rev.* **7**, 1280 (2020).
- [25] C. Hu, K. N. Gordon, P. Liu, J. Liu, X. Zhou, P. Hao, D. Narayan, E. Emmanouilidou, H. Sun, Y. Liu, *et al.*, A van der Waals antiferromagnetic topological insulator with weak interlayer magnetic coupling, *Nat. Commun.* **11**, 97 (2020).
- [26] H. Wang, D. Wang, Z. Yang, M. Shi, J. Ruan, D. Xing, J. Wang, and H. Zhang, Dynamical axion state with hidden pseudospin Chern numbers in MnBi₂Te₄-based heterostructures, *Phys. Rev. B* **101**, 081109 (2020).
- [27] H. Fu, C.-X. Liu, and B. Yan, Exchange bias and quantum anomalous Hall effect in the MnBi₂Te₄/CrI₃ heterostructure, *Sci. Adv.* **6**, eaaz0948 (2020).
- [28] B. Lian, Z. Liu, Y. Zhang, and J. Wang, Flat Chern band from twisted bilayer MnBi₂Te₄, *Phys. Rev. Lett.* **124**, 126402 (2020).
- [29] P. M. Sass, J. Kim, D. Vanderbilt, J. Yan, and W. Wu, Robust A-type order and spin-flop transition on the surface of the antiferromagnetic topological insulator MnBi₂Te₄, *Phys. Rev. Lett.* **125**, 037201 (2020).
- [30] C. Liu, Y. Wang, H. Li, Y. Wu, Y. Li, J. Li, K. He, Y. Xu, J. Zhang, and Y. Wang, Robust axion insulator and Chern insulator phases in a two-dimensional antiferromagnetic topological insulator, *Nat. Mater.* **19**, 522 (2020).
- [31] M. Gu, J. Li, H. Sun, Y. Zhao, C. Liu, J. Liu, H. Lu, and Q. Liu, Spectral signatures of the surface anomalous Hall effect in magnetic axion insulators, *Nat. Commun.* **12**, 3524 (2021).
- [32] H. Li, C.-Z. Chen, H. Jiang, and X. C. Xie, Coexistence of quantum Hall and quantum anomalous Hall phases in disordered MnBi₂Te₄, *Phys. Rev. Lett.* **127**, 236402 (2021).
- [33] A. Gao, Y.-F. Liu, C. Hu, J.-X. Qiu, C. Tzschaschel, B. Ghosh, S.-C. Ho, D. Bérubé, R. Chen, H. Sun, *et al.*, Layer Hall effect in a 2D topological axion antiferromagnet, *Nature* **595**, 521 (2021).
- [34] C. Liu, Y. Wang, M. Yang, J. Mao, H. Li, Y. Li, J. Li, H. Zhu, J. Wang, L. Li, *et al.*, Magnetic-field-induced robust zero Hall plateau state in MnBi₂Te₄ Chern insulator, *Nat. Commun.* **12**, 4647 (2021).
- [35] T. Zhu, H. Wang, and H. Zhang, Floquet engineering of magnetic topological insulator MnBi₂Te₄ films, *Phys. Rev. B* **107**, 085151 (2023).
- [36] Y. Bai, Y. Li, J. Luan, R. Liu, W. Song, Y. Chen, P.-F. Ji, Q. Zhang, F. Meng, B. Tong, L. Li, Y. Jiang, Z. Gao, L. Gu, J. Zhang, Y. Wang, Q.-K. Xue, K. He, Y. Feng, and X. Feng, Quantized anomalous Hall resistivity achieved in molecular beam epitaxy-grown MnBi₂Te₄ thin films, *Nat. Sci. Rev.* **10**, nwad189 (2023).
- [37] N. Wang, D. Kaplan, Z. Zhang, T. Holder, N. Cao, A. Wang, X. Zhou, F. Zhou, Z. Jiang, C. Zhang, S. Ru, H. Cai, K. Watanabe, T. Taniguchi, B. Yan, and W. Gao, Quantum-metric-induced nonlinear transport in a topological antiferromagnet, *Nature* **621**, 487 (2023).
- [38] A. Gao, Y.-F. Liu, J.-X. Qiu, B. Ghosh, T. V. Trevisan, Y. Onishi, C. Hu, T. Qian, H.-J. Tien, S.-W. Chen, M. Huang, D. Bérubé, H. Li, C. Tzschaschel, T. Dinh, Z. Sun, S.-C. Ho, S.-W. Lien, B. Singh, K. Watanabe, T. Taniguchi, D. C. Bell, H. Lin, T.-R. Chang, C. R. Du, A. Bansil, L. Fu, N. Ni, P. P. Orth, Q. Ma, and S.-Y. Xu, Quantum metric nonlinear Hall effect in a topological antiferromagnetic heterostructure, *Science* **381**, 181 (2023).
- [39] T. Zhu, H. Wang, H. Zhang, and D. Xing, Tunable dynamical magnetoelectric effect in antiferromagnetic topological insulator MnBi₂Te₄ films, *npj Comput. Mater.* **7**, 121 (2021).
- [40] W.-Y. Shan, H.-Z. Lu, and S.-Q. Shen, Effective continuous model for surface states and thin films of three-dimensional topological insulators, *New J. Phys.* **12**, 043048 (2010).
- [41] H.-Z. Lu, W.-Y. Shan, W. Yao, Q. Niu, and S.-Q. Shen, Massive Dirac fermions and spin physics in an ultrathin film of topological insulator, *Phys. Rev. B* **81**, 115407 (2010).
- [42] H.-P. Sun, C. M. Wang, S.-B. Zhang, R. Chen, Y. Zhao, C. Liu, Q. Liu, C. Chen, H.-Z. Lu, and X. C. Xie, Analytical solution for the surface states of the antiferromagnetic topological insulator MnBi₂Te₄, *Phys. Rev. B* **102**, 241406 (2020).
- [43] C. Lei, S. Chen, and A. H. MacDonald, Magnetized topological insulator multilayers, *Proc. Natl. Acad. Sci.* **117**, 27224 (2020).
- [44] D. Wang, H. Wang, and H. Zhang, Dirac fermion approach and its application to design high Chern numbers in magnetic topological insulator multilayers, *Phys. Rev. B* **107**, 155114 (2023).
- [45] D. Wang, H. Wang, D. Xing, and H. Zhang, Three-Dirac-fermion approach to unexpected universal gapless surface states in van der Waals magnetic topological insulators, *Sci. China-Phys. Mech. Astron.* **66**, 297211 (2023).
- [46] C.-X. Liu, X.-L. Qi, H. Zhang, X. Dai, Z. Fang, and S.-C. Zhang, Model hamiltonian for topological insulators, *Phys. Rev. B* **82**, 045122 (2010).
- [47] M. Bosnar, A. Y. Vyazovskaya, E. K. Petrov, E. V. Chulkov, and M. M. Otrokov, High Chern number van der Waals magnetic topological multilayers MnBi₂Te₄/hBN, *npj 2D Materials and Applications* **7**, 33 (2023).
- [48] Y. Han, S. Pan, and Z. Qiao, Topological junctions in high-Chern-number quantum anomalous Hall systems, *Phys. Rev. B* **108**, 115302 (2023).
- [49] W. Zhu, C. Song, H. Bai, L. Liao, and F. Pan, High Chern number quantum anomalous Hall effect tunable by stacking order in van der Waals topological insulators, *Phys. Rev. B* **105**, 155122 (2022).

- [50] X. Wan, Z. Ning, D.-H. Xu, R. Wang, and B. Zheng, Photoinduced high-Chern-number quantum anomalous Hall effect from higher-order topological insulators, *Phys. Rev. B* **109**, 085148 (2024).
- [51] F. Viot, R. Hayn, M. Richter, and J. van den Brink, Metacinnabar (β -HgS): A strong 3D topological insulator with highly anisotropic surface states, *Phys. Rev. Lett.* **106**, 236806 (2011).
- [52] W. Zhang, R. Yu, W. Feng, Y. Yao, H. Weng, X. Dai, and Z. Fang, Topological aspect and quantum magnetoresistance of β -Ag₂Te, *Phys. Rev. Lett.* **106**, 156808 (2011).
- [53] G. Kresse and D. Joubert, From ultrasoft pseudopotentials to the projector augmented-wave method, *Phys. Rev. B* **59**, 1758 (1999).
- [54] G. Kresse and J. Furthmüller, Efficient iterative schemes for ab initio total-energy calculations using a plane-wave basis set, *Phys. Rev. B* **54**, 11169 (1996).
- [55] Z. S. Aliev, I. R. Amiraslanov, D. I. Nasonova, A. V. Shevelkov, N. A. Abdullayev, Z. A. Jahangirli, E. N. Orujlu, M. M. Otrokov, N. T. Mamedov, M. B. Babanly, and E. V. Chulkov, Novel ternary layered manganese bismuth tellurides of the MnTe – Bi₂Te₃ system: Synthesis and crystal structure, *J. Alloys Compd.* **789**, 443 (2019).
- [56] D. Xiao, Y. Yao, W. Feng, J. Wen, W. Zhu, X.-Q. Chen, G. M. Stocks, and Z. Zhang, Half-Heusler compounds as a new class of three-dimensional topological insulators, *Phys. Rev. Lett.* **105**, 096404 (2010).
- [57] J. Ruan, S.-K. Jian, H. Yao, H. Zhang, S.-C. Zhang, and D. Xing, Symmetry-protected ideal Weyl semimetal in HgTe-class materials, *Nature Communications* **7**, 11136 (2016).
- [58] N. Marzari and D. Vanderbilt, Maximally localized generalized Wannier functions for composite energy bands, *Phys. Rev. B* **56**, 12847 (1997).
- [59] I. Souza, N. Marzari, and D. Vanderbilt, Maximally localized Wannier functions for entangled energy bands, *Phys. Rev. B* **65**, 035109 (2001).
- [60] G. Pizzi, V. Vitale, R. Arita, S. Blügel, F. Freimuth, G. Géranton, M. Gibertini, D. Gresch, C. Johnson, T. Koretsune, J. Ibañez-Azpiroz, H. Lee, J.-M. Lihm, D. Marchand, A. Marrazzo, Y. Mokrousov, J. I. Mustafa, Y. Nohara, Y. Nomura, L. Paulatto, S. Poncé, T. Ponweiser, J. Qiao, F. Thöle, S. S. Tsirkin, M. Wierzbowska, N. Marzari, D. Vanderbilt, I. Souza, A. A. Mostofi, and J. R. Yates, Wannier90 as a community code: new features and applications, *J. Phys.: Condens. Matter* **32**, 165902 (2020).
- [61] Q. Wu, S. Zhang, H.-F. Song, M. Troyer, and A. A. Soluyanov, Wanniertools: An open-source software package for novel topological materials, *Comput. Phys. Commun.* **224**, 405 (2018).
- [62] See the supplemental materials for the detailed derivation of the intertwined Dirac cones with their low-energy effective Hamiltonians, discussion of the neglected anisotropic coupling, the results for $n = 2, 4, 6$ cases, total energy calculations of MnBi₂Te₄/(Bi₂Te₃)_m/MnBi₂Te₄ ($m = 0, 1, 2$) heterostructures, and the detailed band structures and Wilson loops of cases of $m=0,2$.
- [63] L. Fu, Hexagonal warping effects in the surface states of the topological insulator Bi₂Te₃, *Phys. Rev. Lett.* **103**, 266801 (2009).
- [64] G. Naselli, A. G. Moghaddam, S. Di Napoli, V. Vildosola, I. C. Fulga, J. van den Brink, and J. I. Facio, Magnetic warping in topological insulators, *Phys. Rev. Res.* **4**, 033198 (2022).
- [65] R. C. Vidal, A. Zeugner, J. I. Facio, R. Ray, M. H. Haghghi, A. U. Wolter, L. T. C. Bohorquez, F. Caglieris, S. Moser, T. Figgemeier, *et al.*, Topological electronic structure and intrinsic magnetization in MnBi₄Te₇: A Bi₂Te₃ derivative with a periodic Mn sublattice, *Phys. Rev. X* **9**, 041065 (2019).
- [66] M. Z. Shi, B. Lei, C. S. Zhu, D. H. Ma, J. H. Cui, Z. L. Sun, J. J. Ying, and X. H. Chen, Magnetic and transport properties in the magnetic topological insulators MnBi₂Te₄(Bi₂Te₃)_n ($n = 1, 2$), *Phys. Rev. B* **100**, 155144 (2019).
- [67] J. Wu, F. Liu, M. Sasase, K. Ienaga, Y. Obata, R. Yukawa, K. Horiba, H. Kumigashira, S. Okuma, T. Inoshita, *et al.*, Natural van der Waals heterostructural single crystals with both magnetic and topological properties, *Sci. Adv.* **5**, eaax9989 (2019).
- [68] D. Souchay, M. Nentwig, D. Günther, S. Keilholz, J. de Boor, A. Zeugner, A. Isaeva, M. Ruck, A. U. B. Wolter, B. Büchner, and O. Oeckler, Layered manganese bismuth tellurides with GeBi₄Te₇- and GeBi₆Te₁₀-type structures: Towards multifunctional materials, *J. Mater. Chem. C* **7**, 9939 (2019).
- [69] X. Wu, J. Li, X.-M. Ma, Y. Zhang, Y. Liu, C.-S. Zhou, J. Shao, Q. Wang, Y.-J. Hao, Y. Feng, E. F. Schwier, S. Kumar, H. Sun, P. Liu, K. Shimada, K. Miyamoto, T. Okuda, K. Wang, M. Xie, C. Chen, Q. Liu, C. Liu, and Y. Zhao, Distinct topological surface states on the two terminations of MnBi₄Te₇, *Phys. Rev. X* **10**, 031013 (2020).
- [70] R. C. Vidal, H. Bentmann, J. I. Facio, T. Heider, P. Kagerer, C. I. Fornari, T. R. F. Peixoto, T. Figgemeier, S. Jung, C. Cacho, B. Büchner, J. van den Brink, C. M. Schneider, L. Plucinski, E. F. Schwier, K. Shimada, M. Richter, A. Isaeva, and F. Reinert, Orbital complexity in intrinsic magnetic topological insulators MnBi₄Te₇ and MnBi₆Te₁₀, *Phys. Rev. Lett.* **126**, 176403 (2021).
- [71] W. Ge, J. Kim, Y.-T. Chan, D. Vanderbilt, J. Yan, and W. Wu, Direct visualization of surface spin-flip transition in MnBi₄Te₇, *Phys. Rev. Lett.* **129**, 107204 (2022).
- [72] X. Xu, S. Yang, H. Wang, R. Guzman, Y. Gao, Y. Zhu, Y. Peng, Z. Zang, M. Xi, S. Tian, Y. Li, H. Lei, Z. Luo, J. Yang, Y. Wang, T. Xia, W. Zhou, Y. Huang, and Y. Ye, Ferromagnetic-antiferromagnetic coexisting ground state and exchange bias effects in MnBi₄Te₇ and MnBi₆Te₁₀, *Nat. Commun.* **13**, 7646 (2022).
- [73] A. Alexandradinata, X. Dai, and B. A. Bernevig, Wilson-loop characterization of inversion-symmetric topological insulators, *Phys. Rev. B* **89**, 155114 (2014).

Supplemental Materials for "Symmetry-driven anisotropic coupling effect in antiferromagnetic topological insulator: Mechanism for high-Chern-number quantum anomalous Hall state"

Yiliang Fan¹, Huaiqiang Wang^{2,*}, Peizhe Tang^{3,4}, Shuichi Murakami⁵, Xiangang Wan^{1,6}, Haijun Zhang^{1,6,*}, and Dingyu Xing^{1,6}

¹ *National Laboratory of Solid State Microstructures and School of Physics, Nanjing University, Nanjing 210093, China*

² *School of Physics and Technology, Nanjing Normal University, Nanjing 210023, China*

³ *School of Materials Science and Engineering, Beihang University, Beijing 100191, China*

⁴ *Max Planck Institute for the Structure and Dynamics of Matter, Center for Free Electron Laser Science, Hamburg 22761, Germany*

⁵ *Department of Physics, Tokyo Institute of Technology, Tokyo 152-8551, Japan*

⁶ *Collaborative Innovation Center of Advanced Microstructures, Nanjing University, Nanjing 210093, China*

Contents

I. Detailed solutions of the intertwined Dirac cones	1
II. Low-energy effective Hamiltonians of the intertwined Dirac cones	2
III. Discussion of the other neglected anisotropic coupling	3
IV. Berry curvatures and anomalous Hall conductivities of model with $n = 2, 4, 6$	4
V. The magnetic ground state of $\text{MnBi}_2\text{Te}_4/(\text{Bi}_2\text{Te}_3)_m/\text{MnBi}_2\text{Te}_4$ ($m = 0, 1, 2$)	4
VI. Wilson-loops of $\text{MnBi}_2\text{Te}_4/\text{Bi}_2\text{Te}_3/\text{MnBi}_2\text{Te}_4$	5
VII. Band structures, Wilson-loops, and edge states of $\text{MnBi}_2\text{Te}_4/(\text{Bi}_2\text{Te}_3)_m/\text{MnBi}_2\text{Te}_4$ ($m = 0, 2$)	5
References	5

I. DETAILED SOLUTIONS OF THE INTERTWINED DIRAC CONES

Here, we present the detailed solutions of the intertwined Dirac cones induced by the anisotropic coupling through solving the gap-closing points and critical potentials of the model Hamiltonian without/with the warping term. Without the warping term, the total Hamiltonian is given by

$$H_0 + H_{\text{coup}} = m\tau_z \otimes \sigma_z + u\tau_z \otimes \sigma_0 + v\tau_z \otimes (k_x\sigma_y - k_y\sigma_x) + (\Delta - Bk^2)\tau_x \otimes \sigma_0 + R_1g_n(k_x, k_y)\tau_y \otimes \sigma_0 \quad (\text{S1})$$

where $g_n(k_x, k_y) = (k_+^n - k_-^n)/2i$ and $k_{\pm} = k_x \pm ik_y$. To get the gap-closing points and critical potential, we must first solve the eigenvalue of the Hamiltonian, and the result is shown below

$$\epsilon_{\pm, \alpha} = \pm[m^2 + v^2k^2 + u^2 + (\Delta - Bk^2)^2 + R_1^2g_n^2 + 2(-1)^{\alpha-1}u\sqrt{m^2 + v^2k^2}]^{1/2}, \quad \alpha = 1, 2 \quad (\text{S2})$$

*Electronic address: zhanghj@nju.edu.cn; Electronic address: hqwang@nju.edu.cn

Next, we choose the two energy eigenvalues near the zero energy, i.e. $\epsilon_{\pm,2}$, and let them equal to each other $\epsilon_{+,2} = \epsilon_{-,2}$, we get the critical potential

$$u_0 = \left\{ m^2 + v^2 k^2 - (\Delta - Bk^2)^2 - R_1^2 g_n^2 + 2i \sqrt{(m^2 + v^2 k^2)[(\Delta - Bk^2)^2 + R_1^2 g_n^2]} \right\}^{1/2} \quad (S3)$$

Since the potential u_0 must be real, we naturally have the conditions:

$$\begin{cases} \Delta - Bk^2 = 0 \\ g_n = (k_+^n - k_-^n)/2i = k^n \sin(n\theta) = 0. \end{cases} \quad (S4)$$

Then we can get the gap-closing points (intertwined Dirac-cone points) from the above conditions and substitute them into the expression of u_0 to get the critical potential value. The final results are shown below:

$$\begin{cases} u_0 = \sqrt{m^2 + v^2 \Delta/B} \\ k_0 = \sqrt{\Delta/B} \\ \theta_j = j\pi/n, \quad j = 0, 1, \dots, 2n-1. \end{cases} \quad (S5)$$

When considering the warping term given by

$$H_{\text{warp}} = R_2 w_n(k_x, k_y) \tau_z \otimes \sigma_z, \quad (S6)$$

with $w_n(k_x, k_y) = (k_+^n + k_-^n)/2$, the solutions of the critical potential and gap-closing points can be obtained by substituting m in the above equations with $m(\mathbf{k}) = m + R_2 w_n(k_x, k_y)$. The results are then obtained as

$$\begin{cases} u_{0,j} = \sqrt{\left[m + (-1)^j R_2 (\Delta/B)^{n/2} \right]^2 + v^2 \Delta/B} \\ k_0 = \sqrt{\Delta/B} \\ \theta_j = j\pi/n, \quad j = 0, 1, \dots, 2n-1. \end{cases} \quad (S7)$$

II. LOW-ENERGY EFFECTIVE HAMILTONIANS OF THE INTERTWINED DIRAC CONES

First, we need to derive the two eigenstates of each intertwined Dirac cone located at $k = k_0$ and $\theta = \theta_j$ in the polar coordinates, which are given by

$$\begin{cases} \psi_+ = \left[\frac{ie^{-i\theta_j}(-m + \sqrt{m^2 + k_0^2 v^2})}{k_0 v}, 1, 0, 0 \right]^T \\ \psi_- = \left[0, 0, \frac{ie^{-i\theta_j}(-m + \sqrt{m^2 + k_0^2 v^2})}{k_0 v}, 1 \right]^T \end{cases} \quad (S8)$$

Then, by projecting the four-band full Hamiltonian in Eq. (S1) into the subspace expanded by the above two eigenstates, the two-band effective Hamiltonian up to linear order in momentum is then obtained as

$$\begin{aligned} h(\theta_j) &= \begin{bmatrix} \frac{\langle \psi_+ | H | \psi_+ \rangle}{|\langle \psi_+ | \psi_+ \rangle|} & \frac{\langle \psi_+ | H | \psi_- \rangle}{\sqrt{|\langle \psi_+ | \psi_+ \rangle| |\langle \psi_- | \psi_- \rangle|}} \\ \frac{\langle \psi_- | H | \psi_+ \rangle}{\sqrt{|\langle \psi_+ | \psi_+ \rangle| |\langle \psi_- | \psi_- \rangle|}} & \frac{\langle \psi_- | H | \psi_- \rangle}{|\langle \psi_- | \psi_- \rangle|} \end{bmatrix} \\ &= -2Bk_0 q_\rho \sigma_x + (-1)^j n R_1 k_0^{n-1} q_\theta \sigma_y + \delta u \sigma_z, \end{aligned} \quad (S9)$$

where $q_\rho = k - k_0$, $q_\theta = k_0 \delta\theta$ with $\delta\theta = \theta - \theta_j$ are the momentum measured from the nodal points along the radial and angular directions in the polar coordinates and $\delta u = u - u_0$. Obviously, this effective Hamiltonian describes a Dirac-cone state.

III. DISCUSSION OF THE OTHER NEGLECTED ANISOTROPIC COUPLING

Based on the theory of invariants [1], when considering all symmetry constraints imposed by the preserved C_{nz} [$=\exp(-\frac{i\pi}{n}\sigma_z)$], PT [$=\tau_x \otimes i\sigma_y K$], and $M_x T$ [$=-i\sigma_z K$] symmetries, the most general symmetry-allowed coupling Hamiltonian can be obtained as

$$H_{\text{coup}} = (\Delta - Bk^2)\tau_x \otimes \sigma_0 + R_1 \frac{k_+^n - k_-^n}{2i} \tau_y \otimes \sigma_0 + R_3 \frac{k_+^n + k_-^n}{2} \tau_x \otimes \sigma_0 \quad (\text{S10})$$

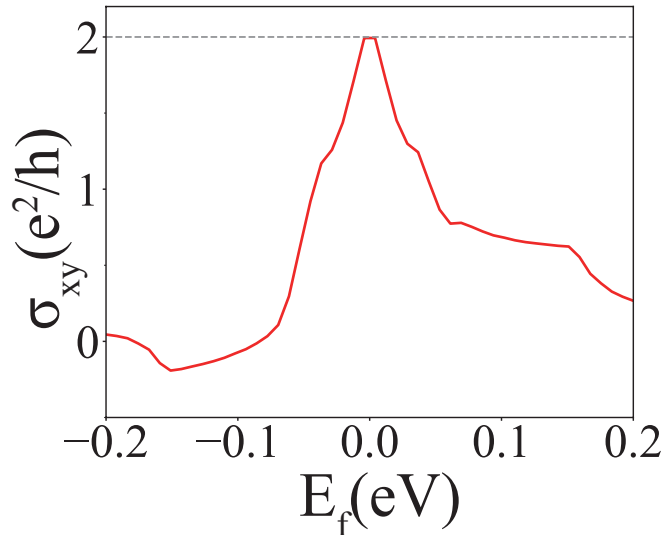


Fig. S1: **Anomalous Hall conductivity for the $n = 2$ case with the neglected R_3 coupling term when $u_- < u < u_+$.** The parameters are chosen as $u = 0.1$ eV, $m = 0.05$ eV, $v = 1$ eV $\cdot \text{\AA}$, $\Delta = 0.05$ eV, $B = 5$ eV $\cdot \text{\AA}^2$, $R_1 = 10$ eV $\cdot \text{\AA}^2$, $R_2 = 10$ eV $\cdot \text{\AA}^2$, $R_3 = 2$ eV $\cdot \text{\AA}^2$ in the above numerical calculations.

Apart from the first two terms discussed in the main text, the third higher-order coupling R_3 term is also symmetry-allowed which is neglected in the main text for simplicity. Here, we will show that it will not affect the main results of our work. We take the $n = 2$ case with the full Hamiltonian written as

$$H = m(\mathbf{k})\tau_z \otimes \sigma_z + u\tau_z \otimes \sigma_0 + v\tau_z \otimes (k_x\sigma_y - k_y\sigma_x) + \Delta(\mathbf{k})\tau_x \otimes \sigma_0 + R_1 g_2(k_x, k_y)\tau_y \otimes \sigma_0, \quad (\text{S11})$$

where $m(\mathbf{k}) = m + R_2(k_x^2 - k_y^2)$, and $\Delta(\mathbf{k}) = \Delta - Bk^2 + R_3(k_x^2 - k_y^2)$. Through a similar procedure as above, we can find the critical potential and the intertwined Dirac cones as

$$\begin{cases} u_+ \equiv u_j = \sqrt{\left(m + \frac{\Delta R_2}{B - R_3}\right)^2 + \frac{v^2 \Delta}{B - R_3}} \\ k_j = \sqrt{\frac{\Delta}{B - R_3}} \\ \theta_j = j\pi/2, \quad j = 0, 2 \end{cases} \quad (\text{S12})$$

and

$$\begin{cases} u_- \equiv u_j = \sqrt{\left(m - \frac{\Delta R_2}{B + R_3}\right)^2 + \frac{v^2 \Delta}{B + R_3}} \\ k_j = \sqrt{\frac{\Delta}{B + R_3}} \\ \theta_j = j\pi/2, \quad j = 1, 3 \end{cases} \quad (\text{S13})$$

As we can see, if $R_3 < B$ is satisfied, there are still two successive gap-closing processes at u_- and u_+ , respectively, and the calculation of anomalous Hall conductivity (AHC) [shown in Fig. S1] confirms that there is a high-Chern-number phase ($|C| = 2$) between u_- and u_+ . However, due to the nonzero R_3 term, the gap-closing points are no

longer located on the circle with radius $k_0 = \sqrt{\Delta/B}$. In contrast, if $R_3 > B$, $k_j = \sqrt{\Delta/(B - R_3)}$ with $j = 0, 2$ will not exist, indicating that there will not be another gap-closing process occurring at $u = u_+$. As a result, there exists an upper critical value of R_3 for the emergence of the intermediate high-Chern-number state. Nevertheless, the R_3 coupling term does not fundamentally affect the results in the main text and is thus reasonably neglected for simplicity.

IV. BERRY CURVATURES AND ANOMALOUS HALL CONDUCTIVITIES OF MODEL WITH $n = 2, 4, 6$

In addition to the $n = 3$ case in the main text, here, we show the numerical calculations of the Berry curvatures and anomalous Hall conductivities for the $n = 2$ (first row), $n = 4$ (second row), and $n = 6$ (third row) cases in Fig. S2.

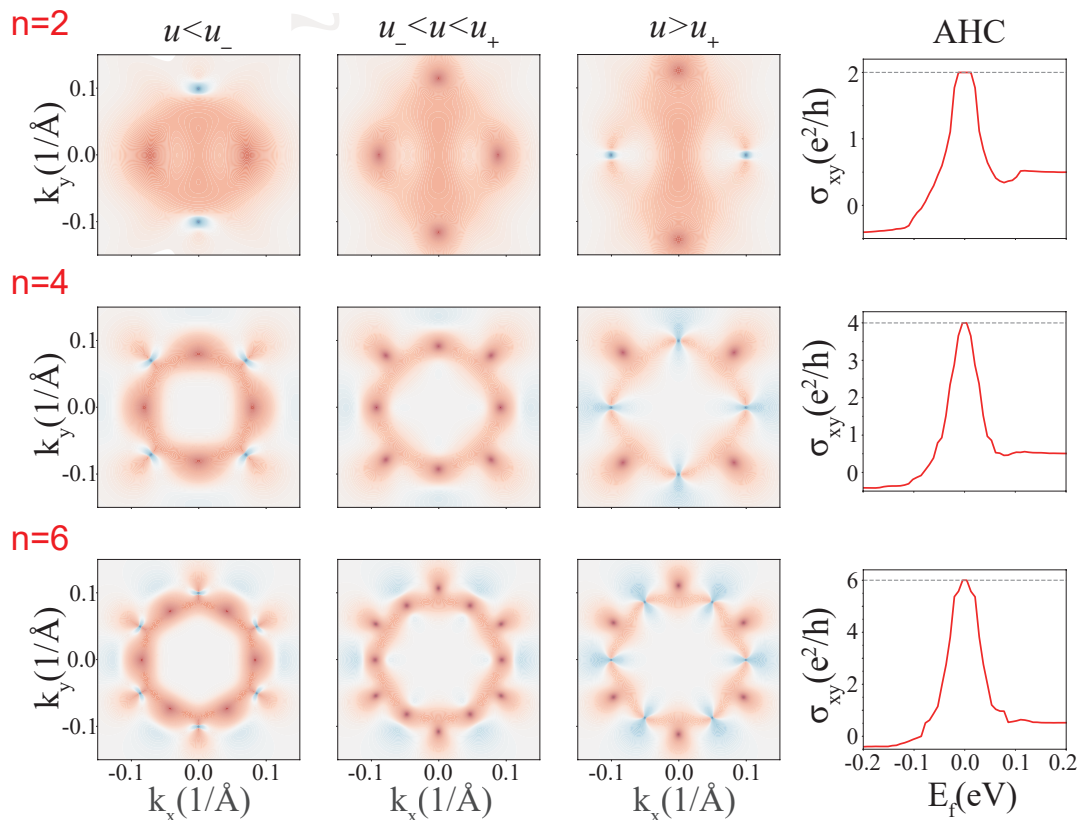


Fig. S 2: **Berry curvatures and anomalous Hall conductivities of model with $n = 2, 4, 6$.** The parameters are chosen as $m = 0.05$ eV, $v = 1$ eV \cdot \AA , $\Delta = 0.05$ eV, $B = 5$ eV \cdot \AA^2 , $R_1 = 10^{n-1}$ eV \cdot \AA^n , $R_2 = 10^{n-1}$ eV \cdot \AA^n in the above numerical calculations.

V. THE MAGNETIC GROUND STATE OF $\text{MnBi}_2\text{Te}_4/(\text{Bi}_2\text{Te}_3)_m/\text{MnBi}_2\text{Te}_4$ ($m = 0, 1, 2$)

Here, we only consider the magnetic order with Mn atoms' magnetic moments towards the out-of-plane direction. We compare the total energy per cell of $\text{MnBi}_2\text{Te}_4/(\text{Bi}_2\text{Te}_3)_m/\text{MnBi}_2\text{Te}_4$ ($m = 0, 1, 2$) with ferromagnetic (FM) order and antiferromagnetic (AFM) order under zero and the typical values of electric field in the calculations. The results are listed in Table S1 and Table S2. As shown in Table S1 (Table S2), for $m=0,1,2$, the total energy per cell of the AFM order is lower than FM order of 1.46 (1.11) meV, 0.19 (5.41) meV and 0.05 (2.97) meV under zero (the typical values of) electric field. These results verify the magnetic ground state of $\text{MnBi}_2\text{Te}_4/(\text{Bi}_2\text{Te}_3)_m/\text{MnBi}_2\text{Te}_4$ ($m = 0, 1, 2$) is AFM order state in the range of electric field of the calculations.

m	Total energy of FM order	Total energy of AFM order
0	0 meV	-1.46 meV
1	0 meV	-0.19 meV
2	0 meV	-0.05 meV

Table S 1: **Total energy per cell of $\text{MnBi}_2\text{Te}_4/(\text{Bi}_2\text{Te}_3)_m/\text{MnBi}_2\text{Te}_4$ ($m = 0, 1, 2$) with out-of-plane FM and AFM magnetic order.** The total energy of the FM order has been set to zero.

m	Electric field	Total energy of FM order	Total energy of AFM order
0	0.015 eV/Å	0 meV	-1.12 meV
1	0.015 eV/Å	0 meV	-5.41 meV
2	0.010 eV/Å	0 meV	-2.97 meV

Table S 2: **Total energy per cell of $\text{MnBi}_2\text{Te}_4/(\text{Bi}_2\text{Te}_3)_m/\text{MnBi}_2\text{Te}_4$ ($m = 0, 1, 2$) with out-of-plane FM and AFM magnetic order under the typical values of electric field.** The total energy of the FM order has been set to zero.

VI. WILSON-LOOPS OF $\text{MnBi}_2\text{Te}_4/\text{Bi}_2\text{Te}_3/\text{MnBi}_2\text{Te}_4$

Here, we show the calculation of the Chern number of $\text{MnBi}_2\text{Te}_4/\text{Bi}_2\text{Te}_3/\text{MnBi}_2\text{Te}_4$ by Wilson-loop methods (the Wilson-loop winding number equals to the Chern number [2]) under different electric field values in Fig. S3. As shown in Fig. S3, when $E = 0.011$ V/Å, the Wilson-loop winding number is 0, when $E = 0.0135$ V/Å, the Wilson-loop winding number is 3, and when $E = 0.0186$ V/Å, the Wilson-loop winding number returns to 0.

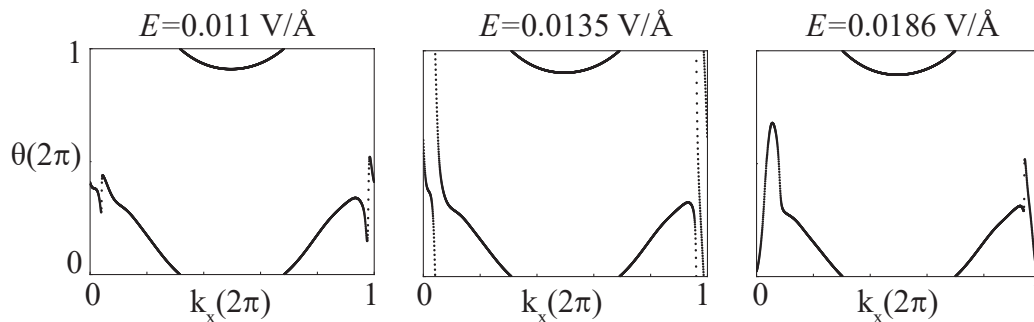


Fig. S 3: **Wilson-loops of $\text{MnBi}_2\text{Te}_4/(\text{Bi}_2\text{Te}_3)/\text{MnBi}_2\text{Te}_4$ under different electric fields.** The electric fields are $E = 0.011$ V/Å, $E = 0.0135$ V/Å, and $E = 0.0186$ V/Å.

VII. BAND STRUCTURES, WILSON-LOOPS, AND EDGE STATES OF $\text{MnBi}_2\text{Te}_4/(\text{Bi}_2\text{Te}_3)_m/\text{MnBi}_2\text{Te}_4$ ($m = 0, 2$)

Here, we show that band structures, Wilson-loops, and edge states of $\text{MnBi}_2\text{Te}_4/(\text{Bi}_2\text{Te}_3)_m/\text{MnBi}_2\text{Te}_4$ ($m = 0, 2$) in Fig. S4 to exhibit the 0-3-0 transition of Chern number of them. Fig. S4a shows band structures of $\text{MnBi}_2\text{Te}_4/(\text{Bi}_2\text{Te}_3)_m/\text{MnBi}_2\text{Te}_4$ ($m = 0, 2$) under different electric fields. For the $m = 0$ ($m = 2$) case, the energy gap closes at $E = 0.0148$ V/Å ($E = 0.0078$ V/Å) and reopens when the electric field continues to increase, and when $E = 0.0168$ V/Å ($E = 0.0125$ V/Å), the gap closes again. Fig. S4c shows the calculation of the Wilson-loops for the $m = 0$ and $m = 2$ cases when $E = 0.0162$ V/Å and $E = 0.01$ V/Å, respectively, both of which exhibit a Wilson-loop winding number of 3. It confirms the existence of a high-Chern-number phase with $C = 3$. Fig. S4b shows the edge states of $m = 0$ and $m = 2$ case when $E = 0.0162$ V/Å and $E = 0.01$ V/Å respectively, verifying the Chern number is indeed 3.

[1] C.-X. Liu, X.-L. Qi, H. Zhang, X. Dai, Z. Fang, and S.-C. Zhang, Phys. Rev. B **82**, 045122 (2010).

[2] A. Alexandradinata, X. Dai, and B. A. Bernevig, Phys. Rev. B **89**, 155114 (2014).

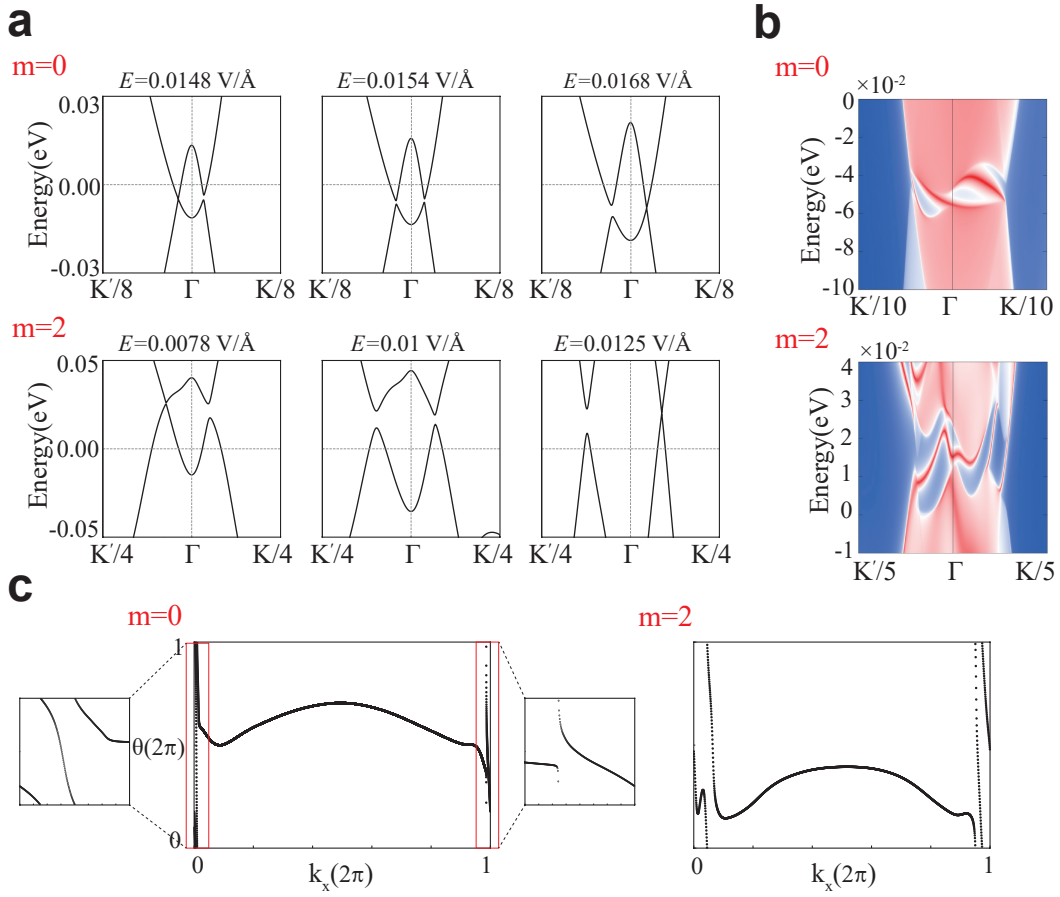


Fig. S 4: **Band structures, Wilson-loops, and edge states of $\text{MnBi}_2\text{Te}_4/(\text{Bi}_2\text{Te}_3)_m/\text{MnBi}_2\text{Te}_4$ ($m = 0, 2$).** (a) Band structures of $\text{MnBi}_2\text{Te}_4/(\text{Bi}_2\text{Te}_3)_m/\text{MnBi}_2\text{Te}_4$ ($m = 0, 2$) under different electric fields: $E = 0.0148 \text{ V/\AA}$, $E = 0.0154 \text{ V/\AA}$, $E = 0.0168 \text{ V/\AA}$ for $m = 0$; $E = 0.0078 \text{ V/\AA}$, $E = 0.01 \text{ V/\AA}$, $E = 0.0125 \text{ V/\AA}$ for $m = 2$. (b) Edge states of $\text{MnBi}_2\text{Te}_4/(\text{Bi}_2\text{Te}_3)_m/\text{MnBi}_2\text{Te}_4$ ($m = 0, 2$) when $E = 0.0162 \text{ V/\AA}$ ($m = 0$) and $E = 0.01 \text{ V/\AA}$ ($m = 2$). (c) Wilson-loops of $\text{MnBi}_2\text{Te}_4/(\text{Bi}_2\text{Te}_3)_m/\text{MnBi}_2\text{Te}_4$ ($m = 0, 2$) when $E = 0.0162 \text{ V/\AA}$ ($m = 0$) and $E = 0.01 \text{ V/\AA}$ ($m = 2$).